ORIGINAL PAPER

On the Development of Equiaxed Microstructures in High-Entropy Superalloys and Their Impact on High-Temperature Oxidation Behavior

Michael J. Pavel[1] · Braeden Duwa[1] · Mark L. Weaver[1]

Abstract

High-Entropy Alloys (HEAs) are an exciting area of research for metallurgists seeking to push through the temperature limits of the traditional nickel- and iron-based superalloys. The HEA design principal is to suppress the formation of low-symmetry phases and maintain a solid solution through the elevated entropy of mixing which is a result of alloying at least four principal elements. Despite early promise, this solid solution-strengthened subsection of HEAs is quite limited in improved operational capacity over dilute alloys with respect to temperature and mechanical behavior. High-Entropy Superalloys (HESAs) refer to those multiple-principal element materials which exhibit secondary strengthening phases such as γ' which has historically allowed nickel-based superalloys to operate near their melting temperatures. As this alloy space is surveyed with arc-melted castings in a high-throughput fashion, potential alloy candidates may be prematurely dismissed based on oxidation behavior without consideration of microstructural uniformity. The Gleeble 3500D thermomechanical simulator was used to develop optimal working parameters for hot thermomechanical processing (HTMP) of the $Ni_{47.5}Fe_{13}Co_{11}Al_{12}Cr_{10}Ta_4Ti_{2.5}$ HESA and create multiple thermogravimetric oxidation specimens. These HTMP samples were compared to solely homogenized specimens and were found to exhibit measurably slower oxidation rates as well as decreased variability in their final performance.

✉ Mark L. Weaver
    mweaver@eng.ua.edu

1   Department of Metallurgical and Materials Engineering,
    University of Alabama, Tuscaloosa, AL 35487-2020, USA

Graphical Abstract
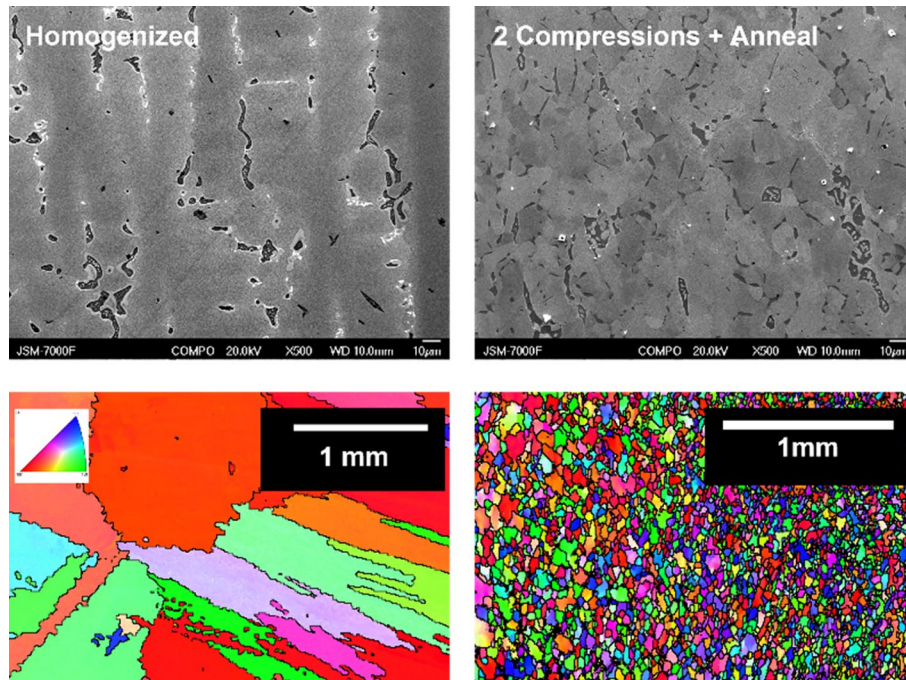
Introduction

High-Entropy Alloys (HEAs) are a group of materials receiving considerable attention due to their unique, highly concentrated compositions, and often impressive mechanical and oxidation resistive properties [1]. These alloys generally consist of five or more elements and have an entropy of mixing greater than 1.5R, where R is the ideal gas constant. From a thermodynamic phase equilibria perspective, the additional entropy of mixing due to multiple concentrated species leads to a suppression of the enthalpic term in the system's total Gibb's free energy, ideally leading to simple single or dual phase microstructures [2]. While the single-phase alloys were the original driving force in the field, it has become apparent that secondary intermetallic phases may not only be beneficial but necessary for maintaining high-temperature properties, similar to the traditional nickel-based superalloys (SAs).

High-Entropy Superalloys (HESAs) are a further development of HEAs which combine the $L1_2$-ordered intermetallic phase of SAs with the additional substitutional alloying of cobalt and iron for nickel, bringing the total composition into the high-entropy space. Compared to SAs, the addition of these transition metals and removal of tungsten, platinum, and rhodium, drastically reduces the

cost and density of the resulting alloy while maintaining most of the high-temperature capabilities [3]. While the addition of cobalt does somewhat increase the alloys' cost, thermodynamic modeling has shown it to be necessary to both stabilize the FCC phases and decrease the total stacking fault energy [4]. The ordered face-centered cubic (FCC) gamma prime (γ') phase, also known by its Strukturbericht designation, $L1_2$, provides the main strengthening mechanism in HESAs and the additions of iron and cobalt have been shown to decrease its total precipitate volume fraction. To counteract this effect, small additions of titanium, niobium, and tantalum have been used to restore the $L1_2$ phase to suitable quantities. The use of thermodynamic modeling to predict the individual effects of each of these elements on the global distribution of phases has proven invaluable and has led to the formation of the composition used in this present study, $Ni_{47.5}Fe_{13}Co_{11}Al_{12}Cr_{10}Ta_4Ti_{2.5}$. This composition has been selected through CALPHAD simulation of the total compositional space using a combination of the nickel alloy (TCNI12) and HEA (TCHEA6) Thermo-Calc™ databases [5, 6].

A problem that arises in the study of new materials—particularly HEAs whose hallmark is chemical breadth—is a lack of understanding the impact of traditional deformation

processing methods (i.e., rolling, forging, extrusion, etc.) on the bulk properties of novel compositions. Key physical attributes such as ductility, strength, toughness, and oxidation behavior are often quantified from small-scale castings and used as high-throughput selection criteria without fully accounting for the non-uniform grain and microstructure development, both of which are known to have tremendous impacts on alloy properties [7]. Oxidation behavior, particularly the growth of Al_2O_3 or Cr_2O_3, is governed by the migration of chemical species along grain boundaries and is, thus, directly tied to the grain boundary density and character of the test specimen [8]. Furthermore, in materials which make use of the secondary phases as solute reservoirs, normalized phase distributions and equilibrium precipitate morphologies should be a requirement for comparative study [9–11]. HEAs that have been produced through arc melting generally consist of highly anisotropic and textured microstructures with grain sizes on the order of millimeters and equally large compositional fluctuations. These regions are large enough that a standard oxidation specimen often exposes 30 or less unique crystallographic orientations to the environment and is, thus, subject to aberrations in the resulting oxidation performance.

This study seeks to highlight the relative ease of small-scale hot thermomechanical process (HTMP) simulation using the Gleeble 3500D or similar load frames to establish stable processing regimes which can be used to generate normalized microstructures in lab-scale environments. To further highlight the benefits of this process, the oxidation performance of the alloy has been evaluated and compared for both the simply homogenized specimens as well as the HTMP alloy.

Experimental Procedure

Approximately 200 g of cast alloy was synthesized through arc melting of pure elemental constituents (purity greater than 99.99%) under an inert ultra-high purity (UHP) argon atmosphere. Cast buttons were flipped and remelted at least five times to ensure complete melting and homogeneity. The large buttons were recast into a cigar shaped mold of approximately 100 mm × 20 mm × 20 mm to allow for efficient cylindrical specimen extraction. The castings were subject to multistage annealing under inert UHP argon which consisted of a 24-hour homogenization at 1000 °C and water quenching, followed by traditional ramped precipitation annealing from 540 °C to 820 °C at 20°C/hour and water quenching.

Crystallographic parameters and bulk chemistry were determined through X-ray diffraction (XRD), energy-dispersive X-ray spectroscopy (EDS) in a scanning electron microscope (SEM), and atom probe tomography (APT) using the LEAP 6000XR and are summarized in Table 1. APT specimens were extracted from the double-compressed and annealed bulk samples and run in laser mode at 30K, 30pJ, 100kHz, and 1% detection rate. Further exploration of the collected APT data will be discussed in a following paper on the bulk oxidation properties and physical metallurgy of the proposed alloy system.

Wire electric discharge machining (EDM) was used to produce cylindrical compression specimens with approximate dimensions of 7 mm (H) by 5 mm (D). To evaluate the high-temperature processability of the alloy, compression tests were conducted in a Gleeble 3500D Thermal–Mechanical Physical simulator at 1000, 1100, and 1200 °C, each at a strain rate of 0.001, 0.01, 0.1, and 0.71 s^{-1} for a total of 12 experimental conditions. Compression testing was performed under strain control and carried out to a total true strain of 0.7 measured via crosshead displacement under inert UHP argon with nickel grease and tantalum shims employed to mitigate barreling due to friction at the sample—anvil interface. The samples were heated at a constant rate of 10 °C/s to the target testing temperature and allowed to thermally equalize for 1 min before undergoing loading. Although direct quenching was not employed, contact between sample and grips was maintained at the conclusion of the test which resulted in an initial cooling rate of approximately 200 °C/s which was estimated from the sample temperature thermocouple data at the conclusion of the test.

The tested compression specimens were cross sectioned via diamond wafering blades, hot mounted in Bakelite™, and metallographically ground and polished through 0.05

Table 1 Bulk/phase chemistry and lattice parameters of the tested material measured by EDS/APT and XRD, respectively

	Lattice Parameter (Å)	Ni (At%)	Co (At%)	Fe (At%)	Cr (At%)	Al (At%)	Ti (At%)	Ta (At%)
Expected Chemistry	–	47.5	11.0	13.0	10.0	12.0	2.5	4.0
Bulk Chemistry (EDS)	–	47.1	11.3	13.3	10.3	11.4	2.5	4.1
FCC Phase (APT)	3.607	33.5	13.5	22.4	20.1	6.9	0.9	1.3
L1$_2$ Phase (APT)	3.597	57.3	9.1	6.0	2.3	14.1	3.7	6.3
BCC Phase (EDS)	2.882	44.9	8.6	8.8	3.9	31.0	1.9	1.0

μm colloidal silica for electron backscatter diffraction (EBSD) analysis. EBSD maps for each sample were collected on an HKL Nordleys detector under a 20keV electron beam in a JEOL 7000 F SEM with larger comparative maps collected with a 2.5 μm step size. HKL Tango was used to process and analyze all of the collected EBSD data to which wild spike removal and 6-nearest-neighbor grain filling were performed. Grain boundaries within the inverse pole figure (IPF) maps were defined with a minimum misorientation of 10° and are lined in black. Kernal Average Misorientation (KAM) maps were calculated with a 3×3 kernel.

XRD was performed using a Philips X'pert MPD with Cu K_α radiation source (45 kV, 40 mA). All measurements were conducted using 9 repeated scans with a step size of 0.008°. Lattice parameters were determined through a whole pattern fitting using the Pawley approach. The extreme texture and overlapping phases make traditional Rietveld refinement quite challenging whereas Pawley fitting allows for the benefit of improved lattice resolution by peak shape matching, while allowing for use of the readily apparent $L1_2$ superlattice reflections without needing to model bulk crystallographic texture [12]. The FCC, $L1_2$, and B2 phases were fit using the Fm $\overline{3}$ m, Pm $\overline{3}$ m, and Pm $\overline{3}$ m space groups, respectively.

Oxidation experiments were conducted at 1000 °C for 50 hours in a 21% pure oxygen atmosphere using a Setaram Setsys Evolution Thermogravimetric Analysis (TGA) system.

Six samples of approximately equal dimensions (L × W × H: 7 mm × 4 mm × 2 mm, Surface Area: 1 cm^2) were used for comparing the effect of HTMP on oxidation behavior. Three were extracted from the originally homogenized casting and three from rectangular specimens which had undergone two orthogonal compressions (1200 °C, $\dot{\varepsilon} = 0.1$ s^{-1}, $\varepsilon_{individual}$

= 0.6) for a total strain of 1.2 followed by 24-h stress relief annealing at 1000 °C and water quenching. The TGA specimens were metallographically mounted and polished prior to oxidation to evaluate the grain structure and texture within each sample via EBSD and XRD. The samples were then removed from their mounts and re-ground to a 600 grit SiC surface finish on all sides. Parabolic oxidation rates were calculated based on the average mass gain for each sample group using the sliding window and complete parabolic fit methodology as described by Monceau and Pieraggi [13].

Results

Figure 1 shows the predicted phase distribution of this HESA as calculated by ThermoCalc and the resulting alloy microstructure after compressions and heat treatment. As predicted, a small volume fraction of aluminum- and nickel-rich regions are precipitated along grain boundaries and were indexed during EBSD as the B2-NiAl. Within the grains themselves, semi-spherical γ′—$L1_2$ precipitates are uniformly distributed throughout the material in a γ-like matrix and were revealed by EDS to be rich in Al, Ni, and Ti, as expected. Although [100]-type B2 superlattice reflections were only observed in XRD of Sample B, thermodynamically, the B2 intermetallic is more stable than BCC for the given composition. The ordered nature of the primary precipitates was confirmed through XRD observation of the [100] and [110] FCC reflections which are forbidden in the disordered FCC structure [14]. These reflections were used in differentiating the $L1_2$ and FCC phases, and the lattice mismatch between matrix and precipitate phases is calculated by Eq. 1 and was found to be -0.28%.

Fig. 1 **a** Simulated one-axis phase diagram for the HESA of interest. **b** Backscatter electron micrograph highlighting the BCC decorated grain boundaries. **c** Grain interior microstructure showing the irregular shaped, high-volume fraction γ′ precipitates within the γ matrix
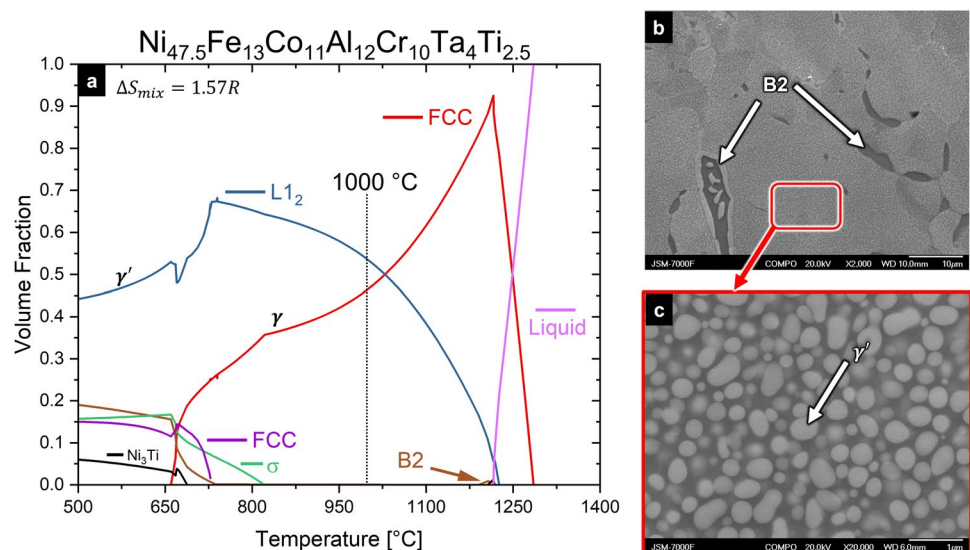
$$\delta = \frac{a_{ppt} - a_{matrix}}{a_{matrix}}. \qquad (1)$$

For γ′-forming alloys, the lattice mismatch and, thus, coherency between precipitate and matrix are responsible for maintaining slow precipitate growth rates and are often range bound to ±1.225% in modern superalloys. Spherical precipitates are often found when δ is between 0 and ± 0.2% whereas the more modern cuboidal shapes are precipitated when δ is greater than 0.5% [7]. The observed irregularly shaped γ′ precipitates are expected given this HESA's intermediate lattice mismatch.

Figure 2 highlights the residual dendritic structure that is present after simple homogenization as well as the evolution of the BCC phase from globular nodules after hot compression to more uniform grain boundary distributions after two compressions and annealing. Further cross-sectional imaging of the oxidized samples from both homogenized and recrystallized groups revealed the recrystallized samples produced a thinner alumina scale after 50 hours of oxidation.

Figure 3 schematically represents the compression and analysis process, and Figure 4 summarizes the hot isothermal compression testing results. Testing revealed the quasi-static compressive yield strength of this HESA to be 250MPa at 1000 °C (approximately $0.8T_{melt}$). As expected, the compressive yield stress increased with strain rate and systematically decreased with increasing temperature. The compressive yield stresses measured for this alloy are somewhat less than to those measured for traditional superalloys [15]. The increased aluminum concentration and removal of refractory and platinum group elements from this alloy
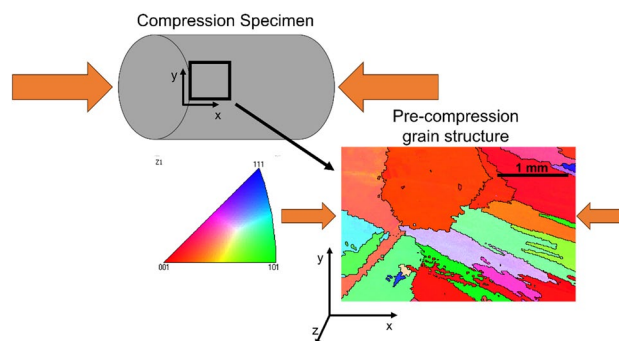

Fig. 3 Schematic diagram of the hot compression of homogenized cylindrical specimens and their representative EBSD IPF map of the pre-strained condition

has led to a depressed melting temperature (~1260 °C) compared to alloys such as CMSX-4 and CM247LC [16, 17].

The systematic decrease in flow stress as a function of strain is indicative of dynamic softening, likely due to the competition of dynamic recovery and recrystallization as dislocations are annihilated and new grains are formed in the straining material. In the highest strain rate samples, discontinuities in the flow stress curves are observed which likely stem from regions of localized failure.

Constitutive Flow Stress Modeling

To assess the deformation behavior of this specific HESA, Zener–Holloman analysis was conducted on the measured compressive flow curves [18]. The Zener–Holloman
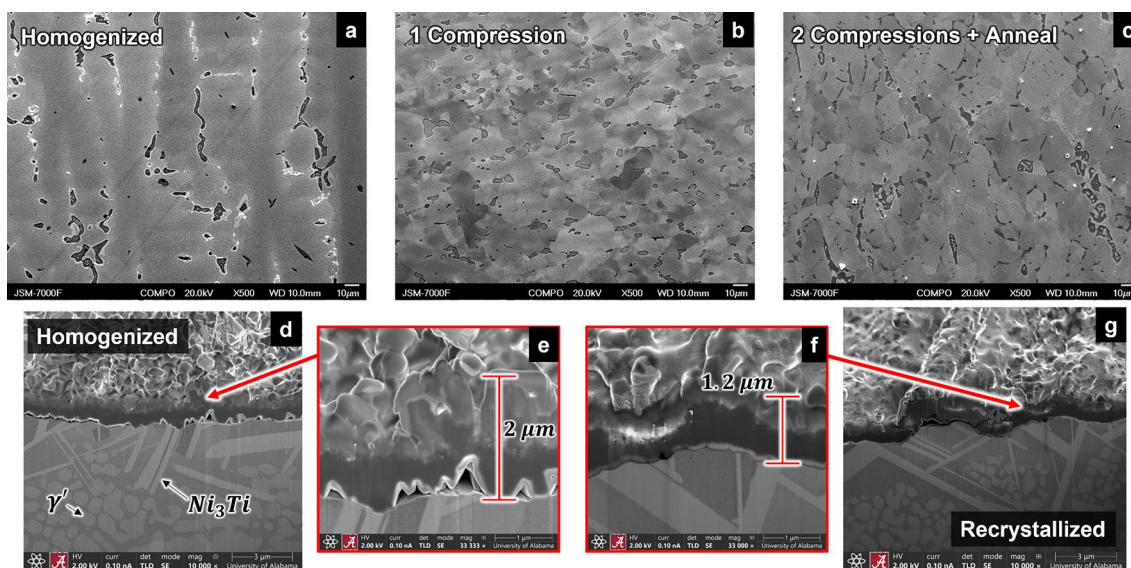
Fig. 2 A series of BSE micrographs showing the final microstructure of the HESA after **a** Homogenization, **b** One 60% strain compression, and **c** Two 60% strain compressions and isothermal annealing. All compressions performed at 1200 °C and 0.1 s^{-1} strain rate. Representative alumina scale cross sections created via focused ion beam for **d**, **e** an as-homogenized sample and **f**, **g** a recrystallized sample
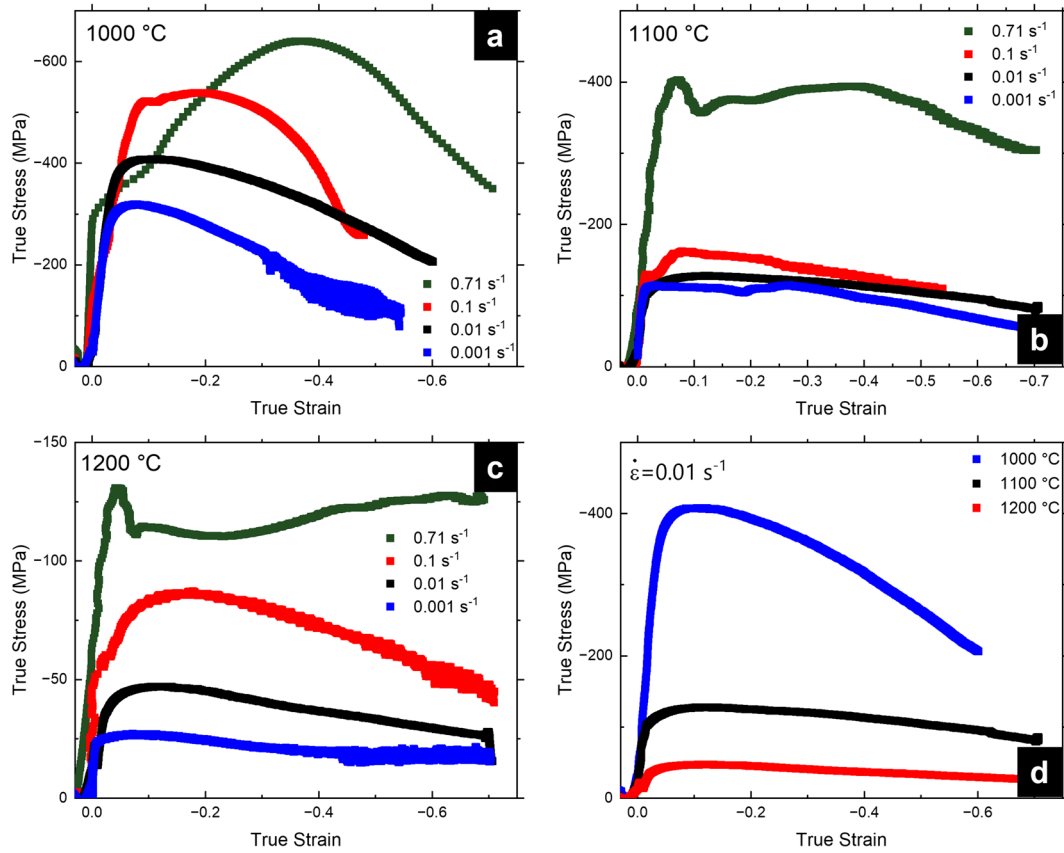
Fig. 4 Resulting hot compression true stress vs. true strain curves collected over four strain rates at **a** 1000 °C, **b** 1100 °C, **c** 1200 °C, and **d** a comparison of mechanical behavior with respect to temperature for the 0.01 s^{-1} strain rate condition

parameter, Z, describes the changes in a material's plastic flow for a given temperature and strain rate:

$$Z = \dot{\varepsilon}\exp\left(\frac{Q}{RT}\right), \tag{2}$$

where $\dot{\varepsilon}$ is the deformation strain rate (s^{-1}), Q is the activation energy for the deformation (kJ/mol), R is the ideal gas constant (kJ/(mol K)), and T is the temperature (degrees K), respectively. Simultaneously, for a fixed, given strain, the flow stress resolved within the specimen can be described by the hyperbolic function first formalized by Sellars and McTegart [19] (Eq. 3). The derivation of its components is described to various levels of detail by several papers [20, 21], and summarized here, in totality:

$$\dot{\varepsilon} = A[\sinh(\alpha\sigma)]^n \exp\left(\frac{-Q}{RT}\right), \tag{3}$$

which may be further reduced by

$$A[\sinh(\alpha\sigma)]^n = \begin{cases} A'\sigma^{n'}, \alpha\sigma < 0.8 \\ A_\beta \exp(\beta\sigma), \alpha\sigma \geq 1.2 \end{cases}, \tag{4}$$

where A, α, n, n′, and β are material parameters derived from the measured flow curves and α = β/n′.

Figure 5 highlights how these parameters are graphically determined through measuring the average slope of the following functions for a fixed, given strain at 1000, 1100, and 1200 °C.
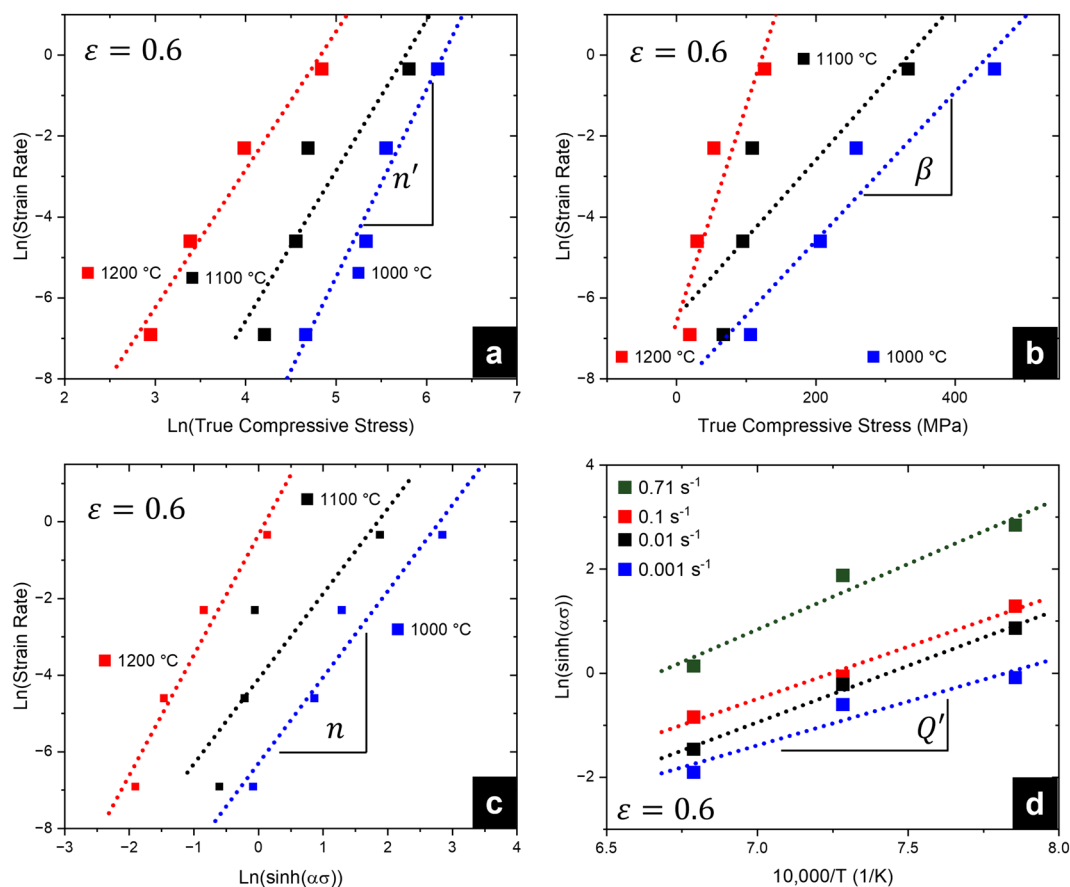
$$n' : \ln(\dot{\varepsilon}) = n'\ln(\sigma) + \ln(A') - Q/RT, \tag{5}$$

$$\beta : \ln(\dot{\varepsilon}) = \beta\sigma + \ln(A_\beta) - Q/RT, \tag{6}$$

$$n : \ln(\dot{\varepsilon}) = n\ln(sinh(\alpha\sigma)) + \ln(A) - Q/RT, \tag{7}$$

$$Q' = \left.\frac{\partial \ln(\sinh(\alpha\sigma))}{\partial\left(\frac{10,000}{T}\right)}\right|_{\dot{\varepsilon}}. \tag{8}$$

$$Q = 10,000R \cdot n \cdot Q', \tag{9}$$

Fig. 5 Graphical derivation of material parameters for this HESA shown at the fixed strain of $\varepsilon = 0.6$. Parameters are derived from the average slope of each linear regression within the sample group. **a** Determination of $n\prime$, **b** determination of β, **c** determination of n, and **d** determination of $Q\prime$

This can be used in turn to calculate the Zener-Hollomon parameter by:

$$\ln(Z) = \ln(A) + n\ln(\sinh(\alpha\sigma)).\tag{10}$$

The activation energy for deformation of the alloy at a strain of 0.6 was found to be 442.1 kJ/mol which is on the upper range of those HEAs studied by Jeong and Kim

Figure 6 summarizes this analysis carried out at for all strains, post-peak stress ($\varepsilon = 0.1$) such that the material parameters α, n, Q, and ln(A) may be modeled as a third-order function of the applied strain and are summarized in Table 2.

To verify those values derived from the measured compressive tests, the predicted theoretical flow stress, σ^{pred}, may be calculated for all strains using the relationships in Table 2 by Eq. 11:

$$\sigma^{pred} = \frac{1}{\alpha} \cdot \ln\left[\left(\frac{Z}{A}\right)^{\frac{1}{n}} + \left[\left(\frac{Z}{A}\right)^{\frac{2}{n}} + 1\right]^{\frac{1}{2}}\right],\tag{11}$$

where temperature and strain rate are accounted for in the Zener-Hollomon parameter (Z) in Equation 2.

Figure 7a shows that the resulting Zener–Hollomon parameter fitting is in reasonable agreement ($R^2 = 0.919$) with the calculated hyperbolic flow stress for the given strain of $\varepsilon = 0.6$. Figure 7b plots the predicted flow stress of this HESA calculated for each temperature, strain rate, and total strain using Eq. 11 against the corresponding experimentally measured stresses. Calculating the correlation between these sets of values yields a Pearson's correlation of R = 0.961 with a 95% confidence interval of [0.946, 0.977]. Residual analysis showed that the data collected at 1100 °C deviated the most from the predicted flow stresses.

The bulk strain rate sensitivity of this alloy, calculated as the inverse of n', ranged between 0.10 and 0.30 which is consistent with other superalloys [22]. This indicates that the deformation is dominated by dislocation climb and glide (rather than superplastic flow) which may ultimately lead to the dynamic recrystallization behavior which is observed in the post-compression microstructures [23].
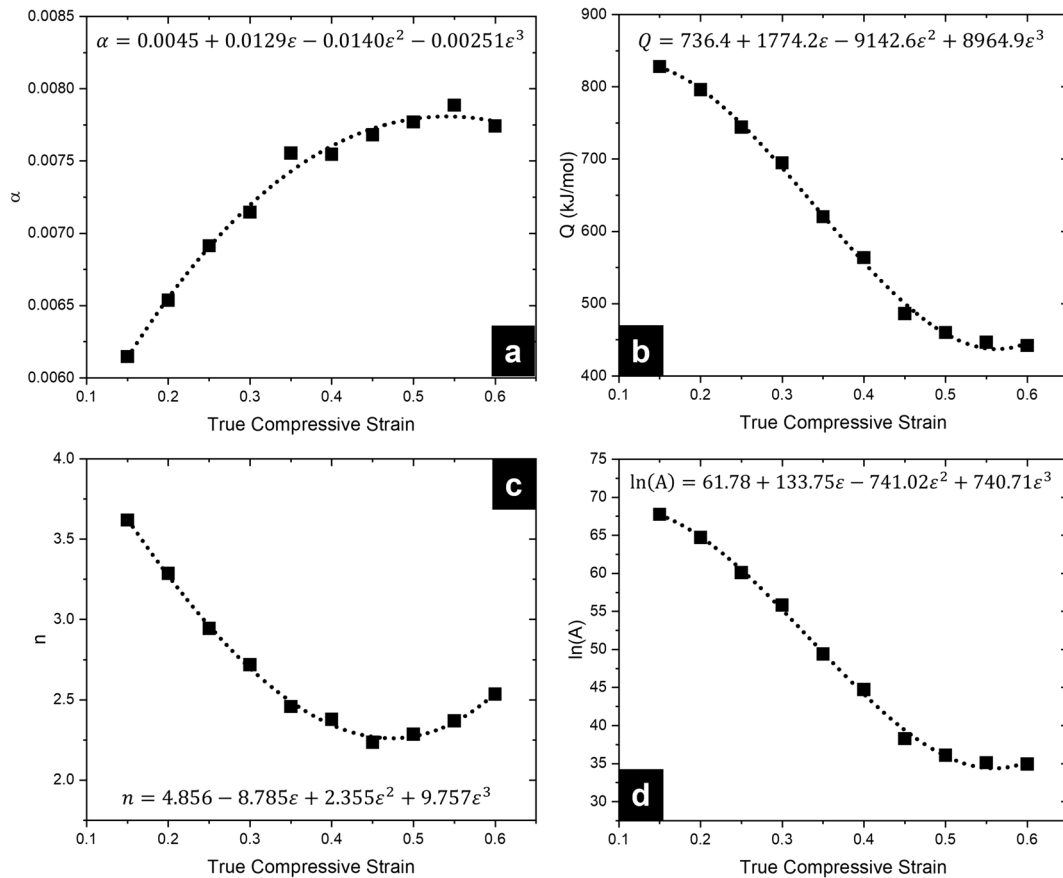
Fig. 6 The following material parameters **a** α, **b** Q, **c** n, and **d** ln(A) are calculated for each amount of strain as described in Fig. 5 and plotted as a function of strain. A third-order polynomial is fit through the resulting data points and is summarized in Table 2

Table 2 Summarized constitutive equations for α, n, Q, and ln(A) as a function of applied strain

$\alpha = 0.0045 + 0.0129\varepsilon - 0.0140\varepsilon^2 - 0.00251\varepsilon^3$

$n = 4.856 - 8.785\varepsilon + 2.355\varepsilon^2 + 9.757\varepsilon^3$

$Q = 736.4 + 1774.2\varepsilon - 9142.6\varepsilon^2 + 8964.9\varepsilon^3$

$\ln(A) = 61.78 + 133.75\varepsilon - 741.02\varepsilon^2 + 740.71\varepsilon^3$

Further processing maps, often used to define temperature, strain, and strain rate regimes which produce stable plastic flow, may be calculated through analysis of the inverse of the power law stress exponent, $n\prime$. The traditional bulk strain rate sensitivity, m, is calculated as the inverse of $n\prime$, which numerically is the inverse slope of ln(Flow Stress) vs ln(Strain Rate) averaged over each testing temperature for a fixed strain. Rather than fitting a simple linear relation for ln(Flow Stress) vs ln(Strain Rate), one may compute a 3rd-order polynomial of ln(Strain Rate) vs ln(Flow Stress), easily calculate its derivate, and easily obtain the strain rate sensitivity now as a function of strain rate and temperature, again at a fixed total strain [24]. Using this relationship, one

may calculate the specific strain rate sensitivity over a range of strain rates and temperatures and apply Murty's criteria for stable flow [25] (Eq. 12):

$$\text{Stability when} : \eta = \frac{2m}{m+1} > 0.285. \tag{12}$$

The ultimate output of this analysis is a contour plot which may assist in determining under which conditions stable plastic flow leading to dynamic recrystallization is more favorable than massive, retained plastic deformation. The validity of a simple polynomial fitting and the application of Murty's deformation efficiency criteria are a somewhat open question for HEAs; however in this case, for high-throughput determination of suitable processing parameters, they were found suitable.

Post-Compression Microstructures

More interesting to the development and future processability of HESAs are the resulting micrographs collected post-compression. Figure 8 shows the IPF-Z EBSD map and
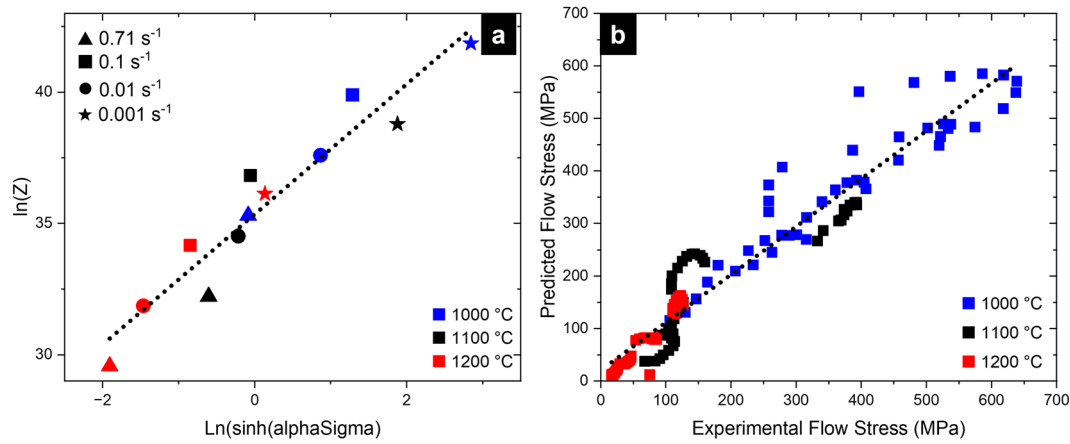
Fig. 7 a To assess the fitting parameters calculated previously, the Zener–Hollomon parameter is plotted against the hyperbolic flow stress at the given strain of $\varepsilon = 0.6$. **b** The derived material parameters as a function of total strain were used to calculate a predicted flow stress of the material and compared to those measured experimentally

Fig. 8 Resulting EBSD IPF maps collected from a representative area within the cross section of each compression specimen. Data are represented in matrix form with fixed temperature by row and fixed strain rate by column
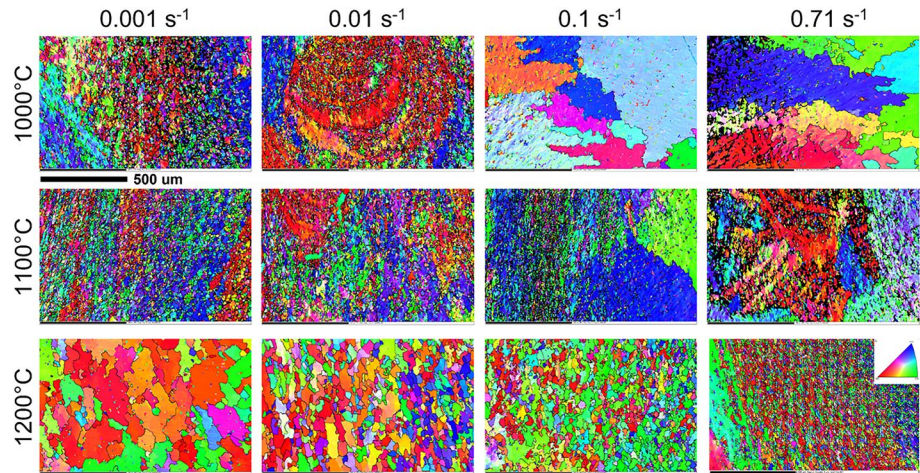
illustrates the alloy's sensitivity to specific deformation conditions which result in recrystallized, randomly distributed, and fine-scale equiaxed grains. Of all the testing conditions, only those conducted at 1200 °C, exceeding 95% of the alloy's predicted melting temperature, produced reasonably uniform recrystallized grain distributions.

For the samples deformed at 1000 °C, discontinues dynamic recrystallization appears to be the dominant recrystallization mechanism in the 0.001 s^{-1} and 0.01 s^{-1} samples due to the presence of small grains along deformation bands. At the higher strain rates, 0.1 and 0.71 s^{-1}, more continuous dynamic recrystallization processes may have taken place as evidenced by the serrated grain edges [26].

At 1100 °C, more complete dynamic recrystallization seems to have taken place, particularly at the lower strain rates. Although the small grains have rotated enough to be indexed as uniquely oriented, a strong texture which resembles the larger parent grains can still be seen throughout the sample, indicative of nucleation and growth in discontinuous dynamic recrystallization [24]. Under faster deformation conditions, the number of unindexed pixels increases, indicative of highly damaged or nanoscale grains [27].

Finally in the samples processed at 1200 °C, complete dynamic recrystallization has occurred in all four strain rate conditions. The slower deformations, 0.001 s^{-1} and 0.01 s^{-1}, have grain structures that resemble recrystallization and subsequent grain growth in contrast to those faster deformation samples which have retained their smaller grain sizes. Dynamic recrystallization is typically inhibited at higher strain rates due to the rapid deformation and cooling that discourages the nucleation and growth of new grains. The reduction in grain size among those 0.1 s^{-1} and 0.71 s^{-1} samples may be, in part, due to post-dynamic recrystallization, a phenomenon seen in when samples are

Fig. 9 Resulting EBSD KAM maps collected from a representative area within the cross section of each compression specimen. Data are represented in matrix form with fixed temperature by row and fixed strain rate by column
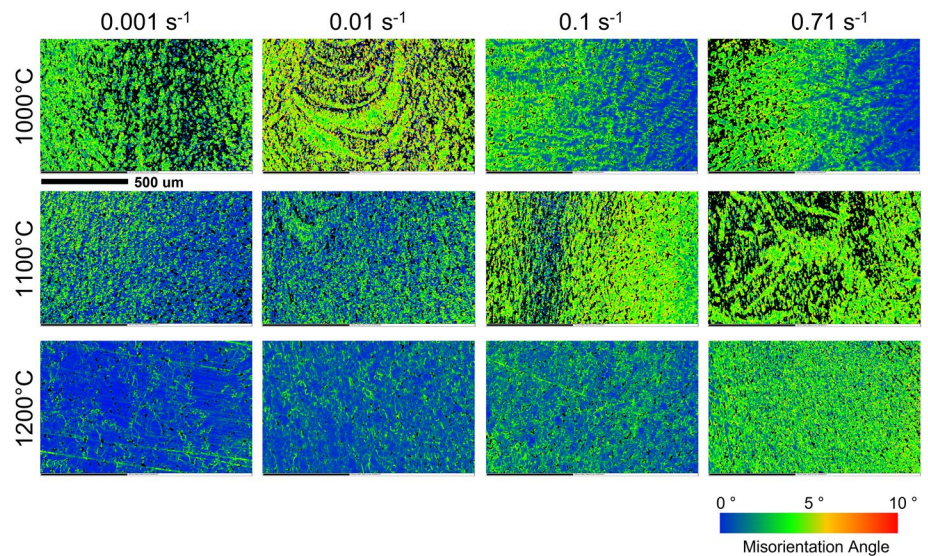
Fig. 10 IPF and KAM EBSD Maps collected for the specimens compressed under **a** 1000 °C at 0.1 s^{-1} and **b** 1200 °C at 0.1 s^{-1}. **c** Processing efficiency maps calculated using polynomial-fit strain rate sensitivity and colored according to the calculated efficiency, η (Eq. 12), with the dashed line separating the 0.285% criteria
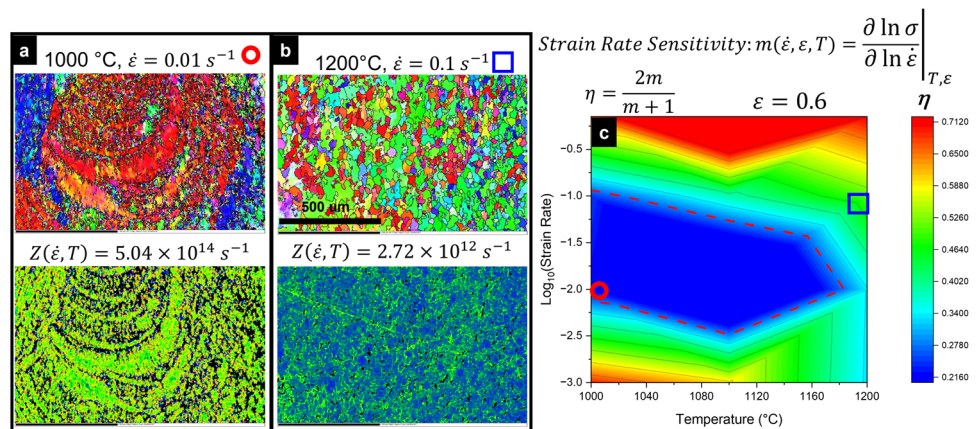
not quenched following compression [28]. The apparent uniformity and reduction in grain size of those samples processed hotter and at faster strain rates is somewhat surprising in the context of classic recrystallization theory but has been previously seen in other nickel-based alloys [15].

Figure 9 exhibits the Kernal Average Misorientation (KAM) maps generated for the testing matrix and highlights the subgrain structure (or lack-thereof) within the deformed grains due to the formation of geometrically necessary dislocations [29, 30]. While the samples compressed at 1000 and 1100 °C show a significant amount of local misorientation (3 − 4° on average), those samples compressed at 1200 °C have much less overall (0 − 2°) and the deformation structures resemble subgrains which may continue to develop under further strain or annealing [31].

Given these results, the condition most suitable for HTMP was 1200 °C at 0.1s^{-1} which displayed smaller amounts of residual damage, maintained small dynamically

recrystallized grains, and was anecdotally found to be the most stable working condition for these samples.

Figure 10 combines the post-compression microstructures for the most obvious retained plastic deformation case (a: 1000 °C at 0.1s^{-1}) and the chosen HTMP condition (b: 1200 °C at 0.1 s^{-1}) with the plastic deformation efficiency criteria (c) calculated in the previous section.

The ideal case for dynamic recrystallization clearly falls outside the band of instability ($\eta < 0.285$) while the retained deformation sample as well as several other conditions presented are clearly within those borders. The calculated Zener–Hollomon parameters for these two conditions also agree with those findings by Jeong and Kim which showed the trend towards dynamic recrystallization as Z approaches and falls below $\sim 10^{12}s^{-1}$. The Z parameter approach provides a more ab initio method of determining suitable processing parameters as it does not require the materials specific strain rate sensitivity and only requires an activation energy which may be found in the literature or generally
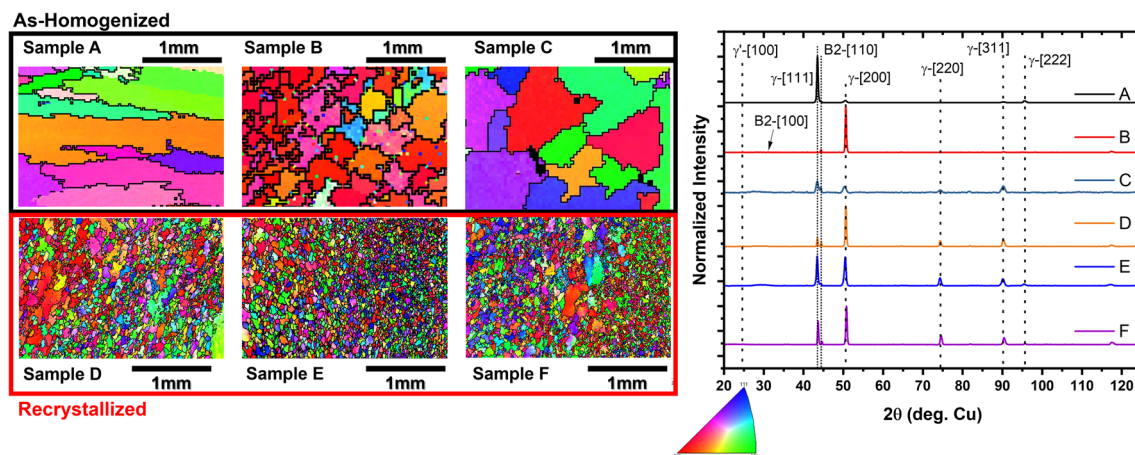
Fig. 11 EBSD IPF maps of three random homogenized TGA specimens (Sample **A**, Sample **B**, and Sample **C**) and three random recrystallized samples (Sample **D**, Sample **E**, and Sample **F**) and their corresponding XRD measurement of the same surface

assumed from the activation energies for diffusion in the alloy of study.

Thermogravimetric Analysis

To fully recrystallize the entire cross section of the bulk specimens under these conditions, rectangular bars were compressed to 60% true strain, re-ground to parallel, and compressed again in a different, orthogonal direction to 60% true strain for a total deformation of 120%.

Figure 11 shows the EBSD maps taken from a representative portion of each simply homogenized and recrystallized (double compression and annealed) TGA sample as well as an XRD measurement taken from the same surface. The standard, homogenized TGA samples exhibited a distinct lack of uniformity, particularly in their crystallographic texture and grain boundary density. Sample A exhibited flattened grains which spanned the entire sample width and while did not exhibit texture in the EBSD IPF-Z maps, was found to be somewhat textured in the [111] direction by XRD. Sample B had a smaller average grain size, and thus, higher grain boundary density, but was shown to be highly textured in the [100] direction by both EBSD and XRD. This extreme texturing proved useful in characterization as the [100] XRD superlattice reflections of the $\gamma\prime$ and B2 phases were most easily observed. Sample C exhibited what might be considered the most uniform grain structure with grain diameters on the order of 1 mm and a more typical orientation distribution seen in EBSD and XRD. The HTMP specimens, labeled Samples D, E, and F, exhibited very similar grain distributions with a smaller average grain size of approximately 40 μm. The more uniform intensity in the XRD patterns and reduction in superlattice reflected intensities indicates a return to a more randomly distributed

grain texture within the samples unlike the as-homogenized series.

Figure 12 shows the TGA results from the homogenized and recrystallized sample groups as well as the comparison of their average performance and respective grain size distributions. The homogenized samples (Fig. 12a) exhibited a significant spread in total mass gain with a total range of 0.1 mg/cm^2, approximately 30% of the overall average specific mass gain. The recrystallized HTMP samples had a total mass gain spread of only 0.07 mg/cm^2 with Sample D and Sample E performing near identically. In turn, when the set of mass gain curves are averaged, the standard deviation of the HTMP samples ($\sigma^{RX} = 0.03$ mg/cm^2) is nearly half that of the homogenized samples ($\sigma^{AH} = 0.05$ mg/cm^2). The overall specific mass gain of the two groups, the recrystallized samples gained less mass overall and in turn exhibited a decreased parabolic oxidation rate, $k_p^{RX} = 2.9 \times 10^{-13}$ (g^2/cm^{4}s), compared to the larger, irregular grained homogenized samples with a measured parabolic oxidation rate of $k_p^{AH} = 5.2 \times 10^{-13}$ (g^2/cm^{4}s).

Discussion

The development of fine grained equiaxed microstructures is essential in the study of all materials, particularly those like HESAs which are generally created at small scales through arc melting. The broader HEA space is often examined in a high-throughput fashion which lends itself towards the testing of as-cast or homogenized specimens which may not be representative of the true material due to the non-equiaxed grain structures developed through columnar grain formation during the ingot's solidification [32]. What may be worse is uninformed hot or cold rolling of the material without further characterization prior to
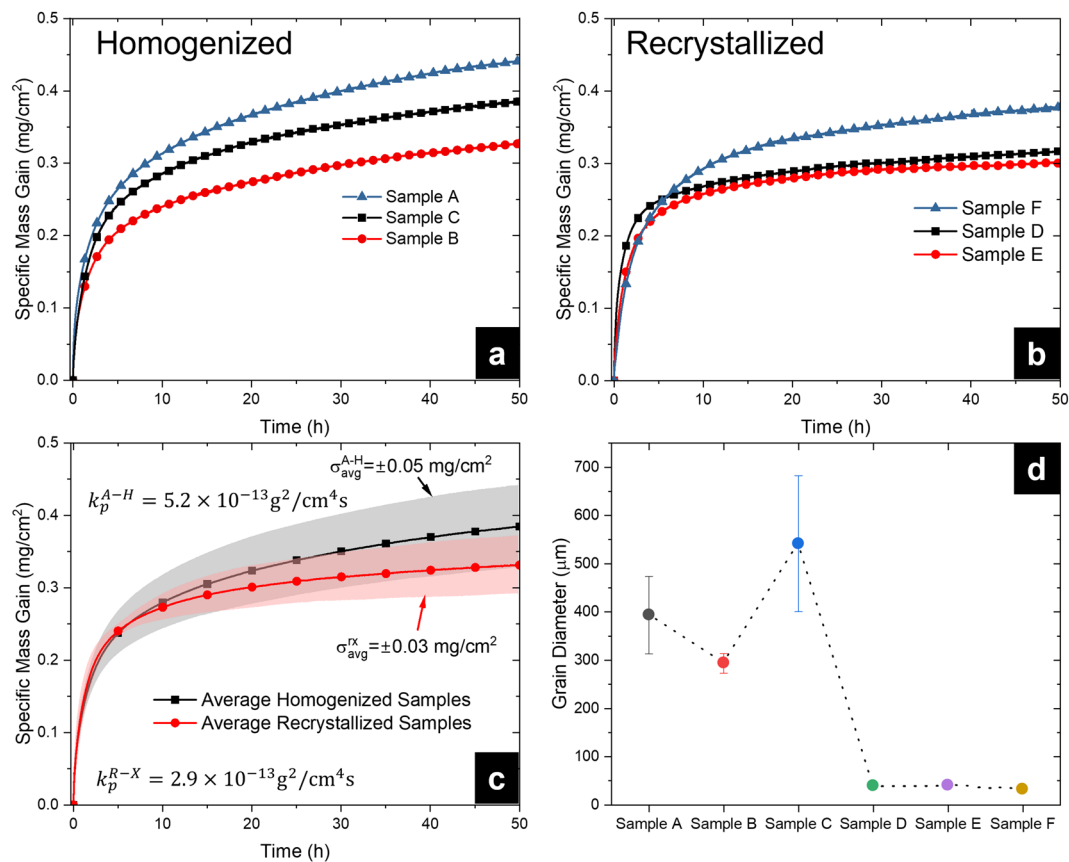
Fig. 12 a Specific mass gain of the homogenized TGA samples A, B, and C. **b** Specific mass gains of the recrystallized TGA samples D, E, and F. **c** Comparative average specific mass gain for the homogenized and recrystallized samples. **d** Grain size distribution for homogenized samples A, B and C and recrystallized samples D, E, and F

testing. The microstructures highlighted in Figs. 8 and 9 show that improper hot working conditions can lead to the development of textures even further from what might be considered isotropic. In the review paper conducted by Jeong and Kim, the study highlighted the fact that many CCA/HEA type materials which had been thermally processed were unable to form fully recrystallized microstructures [33]. Many of the papers reviewed performed recrystallization studies at less than 80% of the alloy melting temperature and correspondingly showed lower degrees of recrystallization. Contrarily, those few which exceeded 80% T_{melt}, including this work, showed some large degree of recrystallization that may be useful in future hot working processes [34, 35]. As explained further in their review, the stability of the hot working process is a fine balance between of materials processing parameters and is reasonably predicted by the n' value calculated in Eq. 5. The authors found that as the homologous temperature is increased beyond 0.8, stable flow tends to prevail, leading to more refined and normalized microstructures [33, 36]. Furthermore, many of the HEAs of study exhibit some degree of nanoscale phase separation which has been shown to disrupt or completely

halt the dynamic recrystallization process [26]. The full homogenization and precipitation heat treatment presented in this study enabled the dissolution of nanoscale phase separation and the major precipitate phase to grow large enough such that the speed of recrystallization may not be severely impacted by short inter-precipitate spacing [26]. Despite the growth of the secondary phase, its presence, coherency, and crystal structure still resist the plastic deformation at elevated temperatures resulting in a relatively high activation energy of 410 kJ/mol as compared to those single-phase HEAs [37] or those MPEAs which contain a major B2 strengthening phase [38]. Despite the thermal stability of the B2 phases, they generally lack the thermally activated change in cross slip plane which provides the yield strength anomaly found in $L1_2$ intermetallics [39] and as such pose a lower barrier to dislocation motion at elevated temperatures compared to $\gamma\prime$ strengthened MPEAs [40].

This alloy sustained outward alumina growth at 1000 °C as expected from the composition which contained approximately 6 wt% and 9 wt% of aluminum and chromium, respectively, and is further characterized in future works. This composition is generally accepted as the

lower limit of critical aluminum concentration needed to sustain external growth for NiCrAl-based alloys [41]. The homogenized alloy series exhibited a significant spread in overall mass gains after 50 hours of exposure. The most and least mass gaining specimens deviated approximately ±15% from the group average. This variability in performance is quite significant when single TGA experiments are used as high-throughput performance metrics. In contrast, the recrystallized specimens varied approximately 10% from their groups average. When comparing the average gains of each group, the recrystallized specimens with smaller grain sizes had a smaller mass gain and lower parabolic oxidation rate (Fig. 12c). This faster conversion to protective oxidation and, thus, increased resistance to mass gain is not unexpected in alumina forming alloys which primarily grow their protective scales via grain boundary grain boundary diffusion. As the smaller-grained underlying alloy exhibits increased grain boundary density, the alumina growth rate is subsequently enhanced [8, 41]. The variability within the homogenized ground broadly coincides with the individual grain size trends for each TGA specimen. Although the effect of texture has not been solely investigated in this study, there is undoubtedly further impact on oxidation from the wide variance in grain boundary misorientation angle distributions and the surface orientation itself.

Conclusion

The formation of small, equiaxed grain microstructures is crucial when determining bulk material properties. This becomes especially important as the broader metallurgy field trends towards determining key material properties from smaller specimens whose measurement field (gage section, surface area, indent footprint, etc.) approaches the grain size of the material. Arc melted samples are particularly susceptible to these issues as they are often the first synthesis path for high-throughput material screening. Using thermomechanical load frames such as the Gleeble 3500D allows for researchers to determine appropriate HTMP routes for generating normalized microstructures prior to small-scale testing. The findings of this research are summarized as follows:

1. Differences in bulk crystallographic texture and grain size lead to significant amounts of variability in TGA-specific mass gains. Reduction of as-homogenized in grain size from approximately 400 µm to 40 µm and increased uniformity in recrystallized microstructures led to decreased mass gain and reduced variability between samples compared to the simply homogenized group. While reducing the grain size and normalizing the samples' microstructures, with respect to arc-melted buttons, are key to producing meaningful and reproducible oxidation parameters, care must be taken to quantify the specimen's grain structure prior to testing.

2. The activation energy for deformation in $Ni_{47.5}Fe_{13}Co_{11}Al_{12}Cr_{10}Ta_4Ti_{2.5}$ was found to vary from 800 to 440 kJ/mol for strains from $\varepsilon = 0.2$ to 0.6, respectively. The hot compressive strength is on the order of more traditional superalloys and exceeds that of Inconel 718 under certain conditions. This elevated activation energy, even at temperatures near melting, is attributed to the retained $\gamma\prime$ which is thermodynamically stable in this alloy through melting and impedes the deformation and recrystallization process.

3. High-entropy superalloys, as with many HEAs, require HTMP at temperatures exceeding 80% T_m, at a minimum, and significant plastic deformation to generate reasonable microstructures. Processing methods such as high-pressure torsion or additive friction stir deposition may offer reasonable solutions to generating small volumes of testing material from arc-melted starting material.

Data Availability The datasets generated and analyzed during the current study are available from the corresponding author on reasonable request.

Declarations

Competing Interest The authors declare that they have no known competing financial interests or personal relationships that could have appeared to influence the work reported in this paper.

References

1. B.S. Murty, J.W. Yeh, S. Ranganathan, P.P. Bhattacharjee, *High entropy alloys*, 2nd edn. (Elsevier, Cambridge, 2019)

2. D.B. Miracle, O.N. Senkov, A critical review of high entropy alloys and related concepts. Acta Mater. (2017). https://doi.org/10.1016/j.actamat.2016.08.081

3. Y.-T. Chen, Y.-J. Chang, H. Murakami, S. Gorsse, A.-C. Yeh, Designing high entropy superalloys for elevated temperature application. Scripta Mater. (2020). https://doi.org/10.1016/j.scriptamat.2020.06.002

4. J.K. Tien, R.N. Jarrett, Effects of cobalt in nickel-base superalloys. High Temp. Alloys Gas Turbines (1982). https://doi.org/10.1007/978-94-009-7907-9_17

5. N. Saunders, A.P. Miodownik, *CALPHAD (calculation of phase diagrams): a comprehensive guide* (Pergamon, Oxford, 1998)

6. J.-O. Andersson, T. Helander, L. Höglund, P. Shi, B. Sundman, Thermo-Calc & DICTRA, computational tools for materials science. Calphad (2002). https://doi.org/10.1016/S0364-5916(02)00037-8

7. M.J. Donachie, S.J. Donachie, *Superalloys: a technical guide* (ASM International, Materials Park, 2002)

8. D.J. Young, *High temperature oxidation and corrosion of metals*, 2nd edn. (Elsevier, Cambridge, 2016)

9. I.G. Wright, V. Nagarajan, J. Stringer, Application of a dispersed-reservoir concept for the development of oxidation-resistant alloys. Corros. Sci. (1993). https://doi.org/10.1016/0010-938X(93)90300-6

10. F. Gesmundo, B. Gleeson, Oxidation of multicomponent two-phase alloys. Oxid. Met. (1995). https://doi.org/10.1007/BF01046728

11. G. Wang, B. Gleeson, D.L. Douglass, A diffusional analysis of the oxidation of binary multiphase alloys. Oxid. Met. (1991). https://doi.org/10.1007/BF00664707

12. G.S. Pawley, Unit-cell refinement from powder diffraction scans. J. Appl. Crystallogr. (1981). https://doi.org/10.1107/S0021888811009618

13. D. Monceau, B. Pieraggi, Determination of parabolic rate constants from a local analysis of mass-gain curves. Oxid. Met. (1998). https://doi.org/10.1023/A:1018860909826

14. Y. Waseda, E. Matsubara, K. Shinoda, *X-Ray diffraction crystallography: introduction, examples and solved problems* (Springer, Heidelberg, 2011)

15. R. Gujrati, C. Gupta, J.S. Jha, S. Mishra, A. Alankar, Understanding activation energy of dynamic recrystallization in Inconel 718. Mater. Sci. Eng., A (2019). https://doi.org/10.1016/j.msea.2018.12.008

16. M. Ramsperger, R.F. Singer, C. Körner, Microstructure of the nickel-base superalloy CMSX-4 fabricated by selective electron beam melting. Metall. and Mater. Trans. A (2016). https://doi.org/10.1007/s11661-015-3300-y

17. J.F.S. Markanday, K.A. Christofidou, J.R. Miller et al., The microstructural evolution of CM247LC manufactured through laser powder bed fusion. Metall. and Mater. Trans. A (2023). https://doi.org/10.1007/s11661-022-06939-0

18. C. Zener, J.H. Hollomon, Effect of strain rate upon plastic flow of steel. J. Appl. Phys. (2004). https://doi.org/10.1063/1.1707363

19. C.M. Sellars, W.J. McTegart, On the mechanism of hot deformation. Acta Metall. (1966). https://doi.org/10.1016/0001-6160(66)90207-0

20. Y. Tong, J.C. Qiao, Y. Yao, The constitutive model and threshold stress for characterizing the deformation mechanism of Al0.3CoCrFeNi high entropy alloy. Mater. Sci. Eng.: A (2018). https://doi.org/10.1016/j.msea.2018.05.109

21. M. Patnamsetty, A. Saastamoinen, M.C. Somani, P. Peura, Constitutive modelling of hot deformation behaviour of a CoCrFeMnNi high-entropy alloy. Sci. Technol. Adv. Mater. (2020). https://doi.org/10.1080/14686996.2020.1714476

22. M. Detrois, S. Antonov, S. Tin, P.D. Jablonski, J.A. Hawk, Hot deformation behavior and flow stress modeling of a Ni-based superalloy. Mater. Charact. (2019). https://doi.org/10.1016/j.matchar.2019.109915

23. S.L. Semiatin, J.M. Shank, A.R. Shiveley, W.M. Saurber, E.F. Gaussa, A.L. Pilchak, The effect of forging variables on the super-solvus heat-treatment response of powder-metallurgy nickel-base superalloys. Metall. and Mater. Trans. A (2014). https://doi.org/10.1007/s11661-014-2572-y

24. N. Ravichandran, Y.V.R.K. Prasad, Dynamic recrystallization during hot deformation of aluminum: a study using processing maps. Metall. Trans. A (1991). https://doi.org/10.1007/bf02665000

25. S.V.S.N. Murty, B.N. Rao, On the development of instability criteria during hotworking with reference to IN 718. Mater. Sci. Eng., A (1998). https://doi.org/10.1016/s0921-5093(98)00764-3

26. F.J. Humphreys, G.S. Rohrer, A.D. Rollett, *Recrystallization and related annealing phenomena*, 3rd edn. (Elsevier, Cambridge, 2017)

27. S. Singh, Y. Guo, B. Winiarski, T.L. Burnett, P.J. Withers, M. De Graef, High resolution low kV EBSD of heavily deformed and nanocrystalline aluminium by dictionary-based indexing. Sci. Rep. (2018). https://doi.org/10.1038/s41598-018-29315-8

28. A. Nicolaÿ, G. Fiorucci, J.M. Franchet, J. Cormier, N. Bozzolo, Influence of strain rate on subsolvus dynamic and post-dynamic recrystallization kinetics of Inconel 718. Acta Mater. (2019). https://doi.org/10.1016/j.actamat.2019.05.061

29. S.I. Wright, M.M. Nowell, D.P. Field, A review of strain analysis using electron backscatter diffraction. Microsc. Microanal. (2011). https://doi.org/10.1017/S1431927611000055

30. N. Harshavardhana, S.P.S.S. Sivam, G. Kumar, A.K. Saxena, A Comparative study on misorientations to determine the extent of recrystallization in pure ETP copper. Phys. Met. Metall. (2021). https://doi.org/10.1134/S0031918X20140094

31. S. Gourdet, F. Montheillet, An experimental study of the recrystallization mechanism during hot deformation of aluminium. Mater. Sci. Eng., A (2000). https://doi.org/10.1016/S0921-5093(00)00733-4

32. M.C. Flemings, Solidification processing. Metall. Trans. (1974). https://doi.org/10.1007/BF02643923

33. H.-T. Jeong, W.J. Kim, Deformation mechanisms and processing maps for high entropy alloys (presentation of processing maps in terms of zener-hollomon parameter): review. Materials (2023). https://doi.org/10.3390/ma16030919

34. M.Z. Ahmed, K. Chadha, S.R. Reddy, D. Shahriari, P.P. Bhattacharjee, M. Jahazi, Influence of process parameters on microstructure evolution during hot deformation of a eutectic high-entropy alloy (EHEA). Metall. and Mater. Trans. A (2020). https://doi.org/10.1007/s11661-020-05991-y

35. T. Cao, L. Ma, L. Wang et al., High temperature deformation behavior of dual-phase Al0.6CoCrFeNi high-entropy alloys. J. Alloys Compd. (2020). https://doi.org/10.1016/j.jallcom.2020.155305

36. H.T. Jeong, H.K. Park, W.J. Kim, Dynamic recrystallization and hot deformation mechanisms of a eutectic Al0.7CoCrFeMnNi high-entropy alloy. J. Alloys Compd. (2021). https://doi.org/10.1016/j.jallcom.2021.159488

37. W.-H. Liao, C.-W. Tsai, Y.-C. Tzeng, W.-R. Wang, C.-S. Chen, J.-W. Yeh, Exploring hot deformation behavior of equimolar CoCrFeNi high-entropy alloy through constitutive equations and microstructure characterization. Mater. Charact. (2023). https://doi.org/10.1016/j.matchar.2023.113234

38. R. John, B.S. Murty, D. Fabijanic, High-temperature deformation behaviour and processing map of near eutectic Al–Co–Cr–Fe–Ni alloy. Intermetallics (2024). https://doi.org/10.1016/j.intermet.2023.108163

39. P.H. Thornton, R.G. Davies, T.L. Johnston, The temperature dependence of the flow stress of the γ′ phase based upon Ni3Al. Metallurgical Transactions (1970). https://doi.org/10.1007/bf02819263

40. T.K. Tsao, A.C. Yeh, C.M. Kuo et al., The high temperature tensile and creep behaviors of high entropy superalloy. Sci. Rep. (2017). https://doi.org/10.1038/s41598-017-13026-7

41. N. Birks, G.H. Meier, F.S. Pettit, *Introduction to the high-temperature oxidation of metals*, 2nd edn. (Campridge University Press, New York, 2006)

Publisher's Note Springer Nature remains neutral with regard to jurisdictional claims in published maps and institutional affiliations.